APL Materials

Strongly enhanced second-order optical nonlinearity in CMOS-compatible $Al_{1-x}Sc_xN$ thin films

Cite as: APL Mater. **9**, 101104 (2021); https://doi.org/10.1063/5.0061787
Submitted: 29 June 2021 . Accepted: 09 September 2021 . Published Online: 04 October 2021

Valerie Yoshioka, Jian Lu, Zichen Tang, et al.

Strongly enhanced second-order optical nonlinearity in CMOS-compatible $Al_{1-x}Sc_xN$ thin films

Cite as: APL Mater. 9, 101104 (2021); doi: 10.1063/5.0061787
Submitted: 29 June 2021 • Accepted: 9 September 2021 •
Published Online: 4 October 2021

Valerie Yoshioka,[1] Jian Lu,[1] Zichen Tang,[2] Jicheng Jin,[1] Roy H. Olsson III,[2] and Bo Zhen[1,a)]

AFFILIATIONS

[1] Department of Physics and Astronomy, University of Pennsylvania, Philadelphia, Pennsylvania 19104, USA
[2] Electrical and Systems Engineering Department, University of Pennsylvania, Philadelphia, Pennsylvania 19104, USA

Note: This paper is part of the Special Topic on Light and Matter Interactions.
[a)] **Author to whom correspondence should be addressed:** bozhen@sas.upenn.edu

ABSTRACT

Silicon photonics has enabled large-scale production of integrated optical devices for a vast array of applications. However, extending its use to nonlinear devices is difficult since silicon does not exhibit an intrinsic second-order nonlinearity. While heterogeneous integration of strongly nonlinear materials is possible, it often requires additional procedures since these materials cannot be directly grown on silicon. On the other hand, CMOS-compatible materials often suffer from weaker nonlinearities, compromising efficiency. A promising alternative to current material platforms is scandium-doped aluminum nitride ($Al_{1-x}Sc_xN$), which maintains the CMOS compatibility of aluminum nitride (AlN) and has been used in electrical devices for its enhanced piezoelectricity. Here, we observe enhancement in optical second-order susceptibility ($\chi^{(2)}$) in CMOS-compatible $Al_{1-x}Sc_xN$ thin films with varying Sc concentrations. For $Al_{0.64}Sc_{0.36}N$, the $\chi^{(2)}$ component d_{33} is enhanced to 62.3 ± 5.6 pm/V, which is 12 times stronger than intrinsic AlN and twice as strong as lithium niobate. Increasing the Sc concentration enhances both $\chi^{(2)}$ components, but loss increases with a higher Sc concentration as well, with $Al_{0.64}Sc_{0.36}N$ exhibiting 17.2 dB/cm propagation loss at 1550 nm and $Al_{0.80}Sc_{0.20}N$ exhibiting 8.2 dB/cm at 1550 nm. Since other material properties of this alloy are also affected by Sc, tuning the Sc concentration can balance strong nonlinearity, loss, and other factors depending on the needs of specific applications. As such, $Al_{1-x}Sc_xN$ could facilitate low cost development of nonlinear integrated photonic devices.

I. INTRODUCTION

Integrated photonics is a growing field that manipulates light signals using compact, chip-sized devices.[1] Far-reaching applications range from telecommunication to sensing to optical computing.[2] While passive devices have proved useful in guiding light, nonlinear devices are capable of controlling interactions between different light signals in more complex processes,[3] widening the capabilities of integrated photonic chips.

Second-order nonlinearities ($\chi^{(2)}$) are used in frequency conversion, modulation, and optical signal processing. Frequency converters shift light sources to particular wavelengths;[4–6] some can tune the source to a desired wavelength within a limited range.[7] Supercontinuum generators broaden spectral width using a combination of nonlinear processes.[8] By shifting signals to desired frequencies, frequency converters can enable communication between systems that operate at different frequencies.[9] Nonlinear interactions can also be observed at a quantum level,[10] allowing single-photon manipulation; in particular, spontaneous parametric down conversion has been used to produce quantum photon pairs.[11] Conversion between RF frequencies and optical frequencies through the linear electro-optic effect can also be considered a $\chi^{(2)}$ nonlinear process; applications include quantum transduction[9,12] and integrated electro-optic modulators.[13] Optical signal processing utilizes nonlinear processes such as difference frequency generation for optical frequency mixing.[14] Furthermore, cascaded $\chi^{(2)}$ processes can act as stronger effective $\chi^{(3)}$ processes for applications that require higher order nonlinear processes, widening their utility. While these processes can be performed with commercial free-space optical components, nonlinear integrated photonic

chips reduce device footprint and enable scalability for complex systems.

Since the crystal structure determines $\chi^{(2)}$ values, nonlinear device performance is often limited by material choice. Additional material limitations include bandgap, absorption loss, ease and cost of fabrication, and compatibility with other materials. An important subset of photonics uses silicon to successfully produce devices on a large scale at low cost using techniques from CMOS facilities. Other CMOS-compatible materials can be grown directly on silicon or electrical chips, decreasing fabrication cost and complexity. Thus, CMOS compatibility is another important consideration that can impact ease and cost of fabrication, particularly on a large scale.

Unfortunately, conflicting limitations can complicate material choice. Silicon is clearly CMOS-compatible, but its centrosymmetric structure precludes it from exhibiting $\chi^{(2)}$ processes; its bandgap of 1.1 eV also results in absorption of visible wavelengths.[15] While many devices use lithium niobate (LN) due to its large $\chi^{(2)}$, with d_{33} = 25 pm/V,[16] it is not compatible with CMOS processes and cannot be directly grown on silicon platforms. Devices that utilize lithium niobate with silicon often utilize wafer bonding, making large-scale production difficult.[17] III–V materials, including GaAs with one of the largest $\chi^{(2)}$ values of d_{36} = 119 pm/V,[16] can be grown on silicon, but most face a multitude of challenges due to lattice mismatch, different thermal expansion coefficients, and high growth temperatures.[18] Several solutions include using buffer layers,[19,20] growing silicon on III–V substrates,[18] and wafer bonding.[21] However, these methods are not always CMOS-compatible and require more complicated fabrication procedures. An exception to this difficulty is the III-nitride class, which could provide a CMOS-compatible option due to their low-temperature sputtering process.[22] However, these materials exhibit lower $\chi^{(2)}$, with AlN's d_{33} = 4 pm/V[23] and GaN's d_{33} = 10.3 pm/V.[24] Furthermore, high-quality GaN samples often use a thin buffer layer of AlN grown on Si first to reduce strain due to differing thermal coefficients.[19,20]

Alloys provide a promising solution to tune and increase $\chi^{(2)}$ while maintaining CMOS compatibility. In particular, substitutional scandium (Sc) in $Al_{1-x}Sc_xN$ alloy thin films adjusts the crystal structure and properties, notably increasing its piezoelectric response.[25] $Al_{1-x}Sc_xN$'s development for electrical devices has resulted in a robust, low-temperature fabrication process that produces high-quality, wafer-scale samples. Unlike many other nonlinear materials, $Al_{1-x}Sc_xN$ is grown at low enough temperatures to be CMOS-compatible and retains a relatively large bandgap. However, its nonlinear optical properties in the visible and near-infrared (NIR) regions have remained largely unexplored. Here, we report enhanced optical $\chi^{(2)}$ of $Al_{1-x}Sc_xN$ thin films based on second harmonic generation (SHG) measurements.

II. FABRICATION

The $Al_{1-x}Sc_xN$ films were deposited in a pulsed DC physical vapor deposition system (Evatec CLUSTERLINE® 200 II) via co-sputtering from separate 4-in. Al and Sc targets at 350C in a pure N_2 environment with a gas flow of 20 SCCM. The power on the Al target was held at 1000 W while the power on the Sc target was adjusted to reach the desired Sc concentration. Calibration of Sc cathode power to Sc concentration was confirmed using energy dispersive x-ray spectroscopy (EDS) in a scanning electron microscope (SEM). High accuracy for the SEM/EDS method is obtained by using a reference sample previously verified by Rutherford Backscattering Spectrometry (RBS) for the k-factor analysis.[26] The samples were grown on 100 mm diameter (100) Si wafers coated with 20 nm of (0001) Ti and 100 nm of (111) Pt. The bulk $Al_{1-x}Sc_xN$ was deposited with c-axis orientation perpendicular to the substrate, targeting a total thickness of 500 nm; the thickness of each sample was confirmed by cross-sectional SEM [Fig. 1(a)].

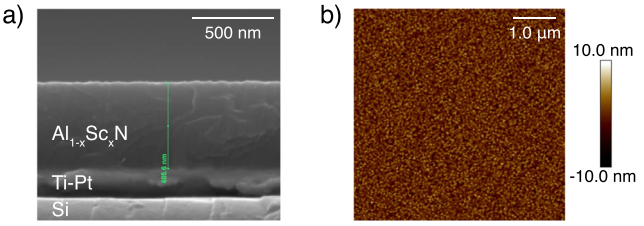

FIG. 1. Thin film characterization. (a) Cross-sectional SEM image of the $Al_{0.64}Sc_{0.36}N$ film, with a thickness of 485.6 nm shown in green. (b) AFM image of the $Al_{0.64}Sc_{0.36}N$ film; no anomalously oriented grains are present. See the supplementary material for SEM and AFM images of all samples.

We confirmed the quality of our samples, even at a high Sc concentration, by AFM imaging Fig. 1(b) and measuring surface roughness and full-width-half-maximum (FWHM) from x-ray diffraction (XRD) rocking curves Table I. The AFM images confirm the lack of anomalously oriented grains,[27] while low roughness over a large, 5 × 5 μm^2 area and consistently sharp XRD curves indicate smooth, highly oriented films.[25] These $Al_{1-x}Sc_xN$ films are nitrogen polar as-deposited as they are readily etched using KOH,[28] unlike metal polar films. Furthermore, large piezoelectric electromechanical coupling has been observed in these $Al_{1-x}Sc_xN$ materials,[29,30] which would be diminished were there alternating domains oriented along the z-axis. As such, these films are strongly oriented and do not exhibit competing domains of opposite polarity. The films are still polycrystalline since in-plane orientation of crystal domains is random despite strong orientation along the direction perpendicular to the substrate. While our samples were grown directly on Pt to enable low-loss reflection SHG, the fabrication process can also be adapted for dielectric substrates, including silicon and sapphire, for low-loss optical and optoelectronic applications.

III. THIN FILM REFLECTION SHG

To determine absolute $\chi^{(2)}$ components, we utilize the relationship between the peak intensity of the fundamental light (I_ω) and SHG ($I_{2\omega}$),[31]

$$I_{2\omega} = \left[\frac{2\omega^2}{\epsilon_0 c^3 n_\omega^2 n_{2\omega}}\right][T_\omega^2 T_{2\omega} T_{2\omega}^{opt}] d_{\text{eff}}^2 I_\omega^2 L^2, \quad (1)$$

where L is the total path length traveled in the sample, T_ω ($T_{2\omega}$) is the polarization-dependent power transmission coefficient of fundamental (SH) light through the air–sample interface, $T_{2\omega}^{opt}$ is the effective power transmission coefficient of SH light through guiding optics after the sample, and d_{eff} is the effective nonlinear coefficient.

TABLE I. Properties of $Al_{1-x}Sc_xN$ films studied in this work. Both rms roughness (R_q) and average roughness (R_a) were measured over a 5 × 5 μm^2 area and are low for all samples, indicating smooth films for optical measurements. Films are relatively thin, ranging around 440–490 nm. The low full-width-half-max (FWHM) of x-ray diffraction (XRD) curves indicates highly oriented films. Refractive indices at 1550 nm (n_ω) and 775 nm ($n_{2\omega}$) slightly increase with the Sc concentration.

Sc (%)	R_q (nm)	R_a (nm)	t (nm)	XRD FWHM (deg)	n_ω	$n_{2\omega}$
0	2.68	2.16	480	1.405	2.05	2.07
10	2.33	1.89	479	1.735	2.06	2.08
20	1.97	1.59	474	1.619	2.14	2.16
28	2.05	1.64	445	1.624	2.15	2.18
36	1.80	1.44	486	1.695	2.21	2.24

Power transmission coefficients were calculated using Fresnel equations; complete reflection from the Pt substrate for both wavelengths was assumed.

The effective nonlinear coefficient d_{eff} is determined by crystal symmetry. $Al_{1-x}Sc_xN$ exhibits a wurtzite structure (6 mm group),[25] so its nonzero $\chi^{(2)}$ components are d_{33}, $d_{31} = d_{32} = d_{15} = d_{24}$ using condensed notation and Kleinman symmetry.[32] In reflection geometry, shown in Fig. 2(a), input polarization (p or s) determines how each component contributes to d_{eff},

$$d_{\text{eff,p}} = d_{33} \times \sin^2\theta_\omega \sin\theta_{2\omega} \times f_p(G_1) + d_{31} \times \cos^2\theta_\omega \sin\theta_{2\omega} \times [2f_p(G_3) + f_p(G_2)], \quad (2)$$

$$d_{\text{eff,s}} = d_{31} \times \sin\theta_{2\omega} \times f_s(G_1), \quad (3)$$

where θ_ω ($\theta_{2\omega}$) is the angle of refraction for fundamental (SH) light and f terms are polarization-dependent correction factors that account for interference and multiple reflections, as defined in Sec. I of the supplementary material. In the absence of interference, these correction factors each equal one, recovering the typical equation for effective $\chi^{(2)}$ components in wurtzite films (Ref. 23). Although the samples are polycrystalline in the crystal plane, the in-plane polarization components of p- and s-polarized fundamental light contribute to the SH signal, which is p-polarized in both cases.

L is calculated using cross-sectional SEM thickness measurements in Table I and angle of refraction. The effective refractive index was determined via ellipsometry and prism coupling (Table I); additional details are provided in Sec. II of the supplementary material. Samples with a higher Sc concentration have a slightly higher refractive index, which is consistent with other measurements of the refractive index.[33] Dispersion is minimal as the difference in the refractive index at the fundamental and SH wavelengths is ~0.02–0.03. Birefringence likewise has a negligible effect; additional details are provided in Sec. III of the supplementary material. By comparing the relative strength of the SH signals induced by p- and s-polarized fundamental light, we extract d_{33} and d_{31} using Eqs. (1)–(3).

We measured the polarization-dependent reflected SHG from each sample using the setup shown in Fig. 2(b). Source light from an optical parametric amplifier pumped by a Yb:KGW laser amplifier (PHAROS, Light Conversion) at 1550 nm with a 159 fs pulse duration and 3 kHz repetition rate was incident upon our samples at an angle of 45°. The focused beam size at the sample surface was 0.01 mm^2 based on knife edge measurements. The polarization was controlled to be either p- or s-polarized using two crossed polarizers. The reflected light signal at 775 nm was directed to a calibrated power sensor for absolute power characterization or a spectrometer

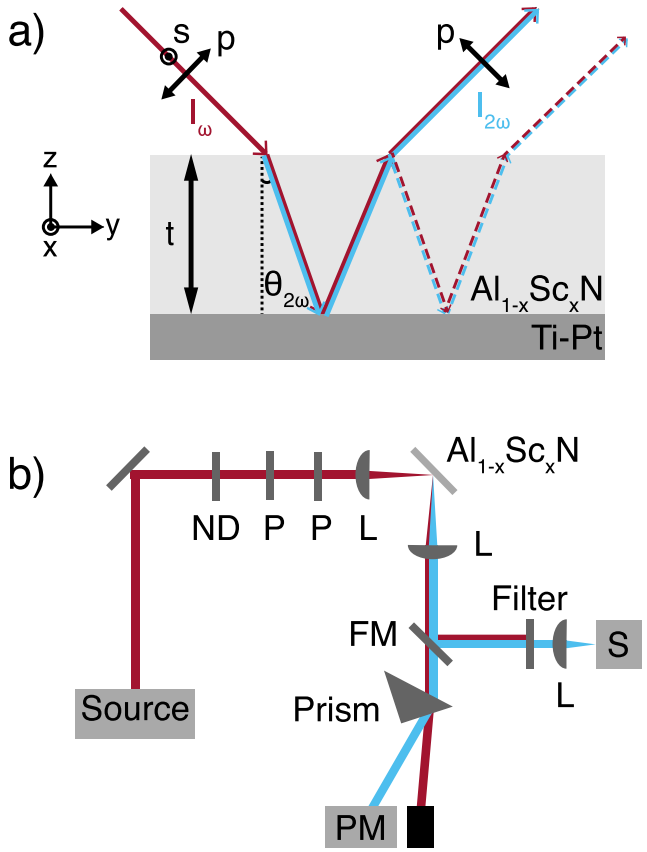

FIG. 2. Schematic of the SHG measurement technique. (a) SHG reflection geometry in the crystal frame of reference. The sample thickness is t, refracted angle of SH light is $\theta_{2\omega}$, and polarization is labeled p and s. The SHG is p-polarized regardless of input polarization due to crystal symmetry. Multiple reflections are shown as their interference has a non-negligible effect. (b) SHG measurement apparatus. *ND*: neutral density filter, *P*: polarizer, *L*: lens, *S*: $Al_{1-x}Sc_xN$ sample, *FM*: flip mirror, *F*: filter, and *PM*: power meter. The SH signal is separated from fundamental light using a high-pass filter or a prism for spectra and power measurements, respectively.

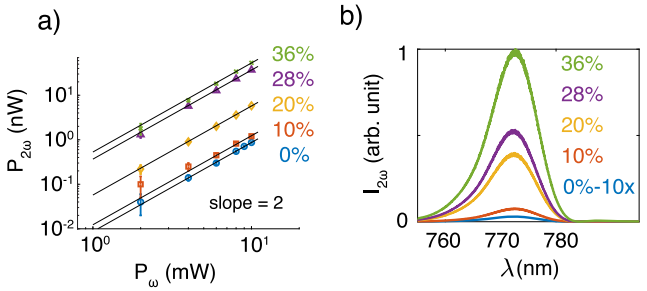

FIG. 3. SHG measurement. (a) SHG power dependence from *p*-polarized input. Black lines indicate quadratic power dependence fits for SH signal for each sample. From bottom to top, data from the 0% Sc sample are indicated by blue circles, 10% by orange squares, 20% by yellow diamonds, 28% by purple triangles, and 36% by green crosses. (b) SH spectra from *p*-polarized input, similarly color coded by the Sc concentration. Samples with a higher Sc concentration exhibit stronger SHG. The signal from the 0% Sc sample has been scaled by a factor of 10 for visibility.

for spectral measurements. All measurements were taken under the same conditions, accounting for sample differences like film thickness and refractive index. We confirmed the quadratic power dependence of the signal for each sample to ensure that the signal was due to perturbative SHG, as shown in Fig. 3(a). The SHG in each sample exhibits *p*-polarization for both *s*- and *p*-polarized fundamental light, as shown in the supplementary material, Fig. 5, corroborating the above SHG analysis. SH spectra in Fig. 3(b) indicate significant dependence on Sc concentration.

The measured d_{33} and d_{31} values for all samples are shown in Fig. 4 and Table II. For intrinsic AlN, we calculate d_{33} = 5.1 ± 0.4 pm/V and d_{31} = 0.07 ± 0.006 pm/V. Other experimental $\chi^{(2)}$ measurements for AlN range from 4[23] to 11 pm/V[34] for d_{33} and smaller values ranging from 0.04[23] to 0.31 pm/V for d_{31}.[35] Thus, our calculations provide reasonable values for d_{33} and d_{31} of AlN. For $Al_{0.64}Sc_{0.36}N$, we observe the largest d_{33} at 62.3 ± 5.6 pm/V, over twice that of LN; its d_{31} = 4.5 ± 0.3 pm/V is also strongly enhanced compared to that of intrinsic AlN.

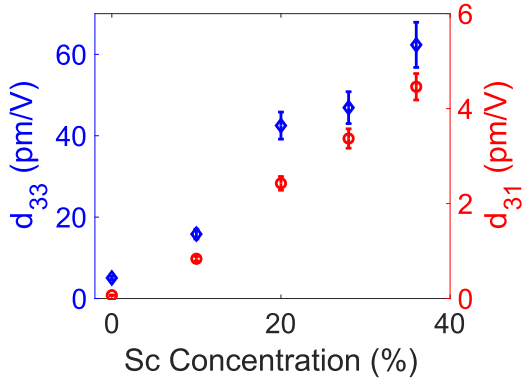

FIG. 4. Experimentally measured d_{33} (blue diamonds) and d_{31} (red circles) as functions of Sc concentration.

TABLE II. $\chi^{(2)}$ values for each sample with different percentages of Sc concentration, where $d_{33} = \chi^{(2)}_{zzz}/2$ and $d_{31} = \chi^{(2)}_{zxx}/2$.

Sc (%)	d_{33} (pm/V)	d_{31} (pm/V)
0	5.1 ± 0.4	0.07 ± 0.006
10	15.8 ± 1.2	0.84 ± 0.05
20	42.5 ± 3.3	2.4 ± 0.1
28	46.9 ± 3.9	3.4 ± 0.2
36	62.3 ± 5.6	4.5 ± 0.3

Although d_{31} is much smaller than d_{33}, its contribution dominates the SH signal induced by p-polarized input light at 45 degree incidence. As a result, the calculated d_{33} value depends strongly on d_{31}, resulting in a higher uncertainty. To better determine d_{33} values in the future, a similar experiment with a larger incidence angle would lower the effect of d_{31} uncertainty on d_{33} values.

Additionally, simulated SH power is strongly dependent on the particular model of Pt utilized. For the analytical calculation described in the Sec. I of the supplementary material, we utilized data from Werner *et al* 2009.[43] As our substrates are sputtered Pt, this material may not perfectly match the model, introducing additional uncertainty that cannot be accounted for in error propagation.

IV. DISCUSSION

The $\chi^{(2)}$ enhancement can be attributed to changes in the crystal structure. $Al_{1-x}Sc_xN$'s enhanced piezoelectricity is attributed to Sc destabilizing AlN's wurtzite structure.[25] In SHG and piezoelectricity, a material polarization is induced by an optical or a mechanical perturbation, respectively. As such, the softened wurtzite structure due to substitutional Sc is expected to cause a large $\chi^{(2)}$ response as well. We expect $\chi^{(2)}$ enhancement to continue until centrosymmetric cubic ScN grains begin to form at Sc concentrations around 43%.[25] It is also possible that this softening in the crystal structure affects the relative strength of $\chi^{(2)}$ components, with a higher Sc concentration inducing a lower ratio of d_{33} compared to d_{31}. Young's or the elastic modulus along the z-axis softens more quickly with the increasing Sc concentration than that along the x-axis, indicating that the Sc concentration affects in-plane and out-of-plane crystal axes to different degrees.[36] Furthermore, the $Al_{1-x}Sc_xN$ piezoelectric coefficients, also written as d_{33} and d_{31}, increase at different rates with a higher Sc concentration.[36] As piezoelectric and $\chi^{(2)}$ coefficients are similarly enhanced by the softened crystal structure, it is possible that this softening could also explain the varying ratios of d_{33} compared to d_{31} depending on the Sc concentration. Further research should explore the effects and determine the optimal Sc concentration to use.

While we directly measured the second-order nonlinear optical susceptibility at optical frequencies, the enhancement from the strained wurtzite structure could persist at lower frequencies in the microwave regime. Since the Pockels coefficient can be expressed in terms of $\chi^{(2)}$ at different frequencies,[31] $Al_{1-x}Sc_xN$ could exhibit a stronger Pockels effect than intrinsic AlN, with potential applications in efficient EO modulators or integrated quantum transducers.

It has also been found that the Sc concentration affects absorption properties in the visible to ultraviolet wavelength range. While

AlN exhibits a large 6 eV bandgap, $Al_{1-x}Sc_xN$ has a smaller bandgap, with high quality $Al_{0.59}Sc_{0.41}N$ displaying a 4.5 eV bandgap and higher absorption at subband gap energies.[33] Sample quality also has a significant effect, since $Al_{0.66}Sc_{0.34}N$ was reported to have a bandgap of 2.94 eV.[37] This was attributed to cubic ScN grain formation at Sc concentrations as low as 20%, which could be due to the differences in the fabrication methods.[33,37] Furthermore, AlN has a direct bandgap, while $Al_{1-x}Sc_xN$'s bandgap is expected to become indirect past concentrations of 23% Sc based on a larger measured optical bandgap compared to theoretical predictions.[33]

Applications that utilize longer wavelengths would be minimally affected by the change in the bandgap. Measurements of $Al_{0.85}Sc_{0.15}N$ photonic waveguides indicate losses of 9 ± 2 dB/cm at 1550 nm; however, optimizing the etching process is expected to significantly reduce sidewall roughness and loss.[38] We performed prism coupling measurements of propagation loss for a wafer of $Al_{0.64}Sc_{0.36}N$ on sapphire, which indicate losses around 17.2 dB/cm at 1550 nm, and higher loss above 30 dB/cm at 633 nm. For an $Al_{0.80}Sc_{0.20}N$ sample, the loss at 1550 nm is much lower, around 8.2 dB/cm, with loss above 30 dB/cm at 633 nm as well. Although relatively high, these propagation loss measurements provide an upper estimate of loss from absorption and may be improved by optimizing grain structure. Thus, $Al_{1-x}Sc_xN$ can be used in waveguides and other on-chip optical elements; further improvements in fabrication techniques could lead to reduced propagation loss. For applications at shorter wavelengths, lower Sc concentrations could enhance $\chi^{(2)}$ with less effect on absorption. Further investigation is necessary to determine loss in $Al_{1-x}Sc_xN$ structures at different Sc concentrations and how its absorption affects applications in different wavelength regimes.

Another consideration is quasi-phase matching. While modal phase matching can enable high performance devices, it requires precise waveguide design and adds further constraints. Thus, many devices opt instead to use ferroelectric nonlinear materials, such as LN, which can be periodically poled to achieve quasi-phase matching. While periodic poling of non-ferroelectric materials is possible through doping and other fabrication techniques,[39] it requires additional complicated techniques. Devices with AlN have typically used modal phase matching, but $Al_{1-x}Sc_xN$ is ferroelectric even at low Sc concentrations,[40,41] which could enable periodic poling in $Al_{1-x}Sc_xN$ thin films. The films studied in this work were grown using identical processes to $Al_{1-x}Sc_xN$ films exhibiting ferroelectric switching with poling parameters given in Refs. 28 and 42, indicating the possibility of periodic poling for quasi-phase matching in these films.

V. CONCLUSION

In conclusion, we measured SHG from $Al_{1-x}Sc_xN$ alloy thin films and reported significant enhancement of $\chi^{(2)}$ values with the increasing Sc concentration, up to a factor nearing 12 for $Al_{0.64}Sc_{0.36}N$. Films were fabricated using a low temperature, CMOS-compatible procedure; characterization with AFM and XRD confirms high-quality, well-oriented polycrystalline films. Despite the decrease in the bandgap with the addition of Sc, we expect this material to still be applicable for devices operating at NIR wavelengths. Furthermore, controlling the Sc concentration tunes material properties such as $\chi^{(2)}$ and loss to suit individual applications. As a CMOS-compatible material, $Al_{1-x}Sc_xN$ could more easily combine cutting-edge nonlinear technology with mature silicon photonics and enable large-scale production of integrated nonlinear devices, ranging from on-chip frequency converters to single-photon sources. Future studies will improve etching processes to produce high-quality passive photonic elements, reduce absorption and waveguide loss, and produce devices including nonlinear waveguides and modulators.

SUPPLEMENTARY MATERIAL

See the supplementary material for the full derivation of absolute $\chi^{(2)}$ value, as well as additional information on ellipsometry, dispersion, and birefringence. Figures of SH spectra for both input polarizations, SH polarization, SEM images, and AFM images for all samples are also included.

ACKNOWLEDGMENTS

This work was funded by NSF CAREER Award No. 1944248, Army Research Office (Grant No. W911NF-18-2-0048), and the Office of Naval Research (Grant No. N00014-20-1-2325). V.Y. is a recipient of the Department of Defense National Defense Science and Engineering Graduate (NDSEG) Fellowship and acknowledges the support from this fellowship. Fabrication and characterization were performed at the Singh Center for Nanotechnology at the University of Pennsylvania. Prism coupling measurements were performed by Metricon Corporation.

The authors and the University of Pennsylvania have U.S. provisional patent application 63/227501 pending.

AUTHOR DECLARATIONS

Conflict of Interest

The authors have no conflicts to disclose.

DATA AVAILABILITY

The data that support the findings of this study are available from the corresponding author upon reasonable request.

REFERENCES

[1] G. Lifante, *Integrated Photonics: Fundamentals* (John Wiley & Sons, Ltd., 2003).
[2] L. Thylén and L. Wosinski, "Integrated photonics in the 21st century," Photonics Res. **2**, 75–81 (2014).
[3] S. Fathpour, "Heterogeneous nonlinear integrated photonics," IEEE J. Quantum Electron. **54**, 1–16 (2018).
[4] R. Luo, H. Jiang, S. Rogers, H. Liang, Y. He, and Q. Lin, "On-chip second-harmonic generation and broadband parametric down-conversion in a lithium niobate microresonator," Opt. Express **25**, 24531–24539 (2017).
[5] J.-Y. Chen, Z.-H. Ma, Y. M. Sua, Z. Li, C. Tang, and Y.-P. Huang, "Ultra-efficient frequency conversion in quasi-phase-matched lithium niobate microrings," Optica **6**, 1244–1245 (2019).
[6] J. Lu, J. B. Surya, X. Liu, A. W. Bruch, Z. Gong, Y. Xu, and H. X. Tang, "Periodically poled thin-film lithium niobate microring resonators with a second-harmonic generation efficiency of 250,000%/W," Optica **6**, 1455–1460 (2019).
[7] A. W. Bruch, X. Liu, J. B. Surya, C.-L. Zou, and H. X. Tang, "On-chip $\chi^{(2)}$ microring optical parametric oscillator," Optica **6**, 1361–1366 (2019).

[8]C. R. Phillips, C. Langrock, J. S. Pelc, M. M. Fejer, J. Jiang, M. E. Fermann, and I. Hartl, "Supercontinuum generation in quasi-phase-matched $LiNbO_3$ waveguide pumped by a Tm-doped fiber laser system," Opt. Lett. **36**, 3912–3914 (2011).
[9]T. P. McKenna, J. D. Witmer, R. N. Patel, W. Jiang, R. V. Laer, P. Arrangoiz-Arriola, E. A. Wollack, J. F. Herrmann, and A. H. Safavi-Naeini, "Cryogenic microwave-to-optical conversion using a triply resonant lithium-niobate-on-sapphire transducer," Optica **7**, 1737–1745 (2020).
[10]P. Kumar, "Quantum frequency conversion," Opt. Lett. **15**, 1476–1478 (1990).
[11]X. Guo, C.-l. Zou, C. Schuck, H. Jung, R. Cheng, and H. X. Tang, "Parametric down-conversion photon-pair source on a nanophotonic chip," Light: Sci. Appl. **6**, e16249 (2017).
[12]L. Fan, C.-L. Zou, R. Cheng, X. Guo, X. Han, Z. Gong, S. Wang, and H. X. Tang, "Superconducting cavity electro-optics: A platform for coherent photon conversion between superconducting and photonic circuits," Sci. Adv. **4**, eaar4994 (2018).
[13]C. Xiong, W. H. P. Pernice, and H. X. Tang, "Low-loss, silicon integrated, aluminum nitride photonic circuits and their use for electro-optic signal processing," Nano Lett. **12**, 3562–3568 (2012).
[14]C. Langrock, S. Kumar, J. E. McGeehan, A. E. Willner, and M. M. Fejer, "All-optical signal processing using $\chi^{(2)}$ nonlinearities in guided-wave devices," J. Lightwave Technol. **24**, 2579–2592 (2006).
[15]J. Leuthold, C. Koos, and W. Freude, "Nonlinear silicon photonics," Nat. Photonics **4**, 535–544 (2010).
[16]I. Shoji, T. Kondo, A. Kitamoto, M. Shirane, and R. Ito, "Absolute scale of second-order nonlinear-optical coefficients," J. Opt. Soc. Am. B **14**, 2268–2294 (1997).
[17]L. Chang, M. H. P. Pfeiffer, N. Volet, M. Zervas, J. D. Peters, C. L. Manganelli, E. J. Stanton, Y. Li, T. J. Kippenberg, and J. E. Bowers, "Heterogeneous integration of lithium niobate and silicon nitride waveguides for wafer-scale photonic integrated circuits on silicon," Opt. Lett. **42**, 803–806 (2017).
[18]R. Cariou, W. Chen, J.-L. Maurice, J. Yu, G. Patriarche, O. Mauguin, L. Largeau, J. Decobert, and P. Roca i Cabarrocas, "Low temperature plasma enhanced CVD epitaxial growth of silicon on GaAs: A new paradigm for III-V/Si integration," Sci. Rep. **6**, 25674 (2016).
[19]I. Roland, Y. Zeng, Z. Han, X. Checoury, C. Blin, M. El Kurdi, A. Ghrib, S. Sauvage, B. Gayral, C. Brimont, T. Guillet, F. Semond, and P. Boucaud, "Near-infrared gallium nitride two-dimensional photonic crystal platform on silicon," Appl. Phys. Lett. **105**, 11104 (2014).
[20]N. Vico Triviño, U. Dharanipathy, J.-F. Carlin, Z. Diao, R. Houdré, and N. Grandjean, "Integrated photonics on silicon with wide bandgap GaN semiconductor," Appl. Phys. Lett. **102**, 081120 (2013).
[21]L. Chang, A. Boes, X. Guo, D. T. Spencer, M. J. Kennedy, J. D. Peters, N. Volet, J. Chiles, A. Kowligy, N. Nader, D. D. Hickstein, E. J. Stanton, S. A. Diddams, S. B. Papp, and J. E. Bowers, "Heterogeneously integrated GaAs waveguides on insulator for efficient frequency conversion," Laser Photonics Rev. **12**, 1800149 (2018).
[22]C. Xiong, W. H. P. Pernice, X. Sun, C. Schuck, K. Y. Fong, and H. X. Tang, "Aluminum nitride as a new material for chip-scale optomechanics and nonlinear optics," New J. Phys. **14**, 095014 (2012).
[23]G. T. Kiehne, G. K. L. Wong, and J. B. Ketterson, "Optical second-harmonic generation in sputter-deposited AlN films," J. Appl. Phys. **84**, 5922–5927 (1998).
[24]N. A. Sanford, A. V. Davydov, D. V. Tsvetkov, A. V. Dmitriev, S. Keller, U. K. Mishra, S. P. DenBaars, S. S. Park, J. Y. Han, and R. J. Molnar, "Measurement of second order susceptibilities of GaN and AlGaN," J. Appl. Phys. **97**, 053512 (2005).
[25]M. Akiyama, T. Kamohara, K. Kano, A. Teshigahara, Y. Takeuchi, and N. Kawahara, "Enhancement of piezoelectric response in scandium aluminum nitride alloy thin films prepared by dual reactive cosputtering," Adv. Mater. **21**, 593–596 (2009).
[26]B. Fultz and J. M. Howe, *Transmission Electron Microscopy and Diffractometry of Materials* (Springer Science & Business Media, 2012).
[27]S. Fichtner, N. Wolff, G. Krishnamurthy, A. Petraru, S. Bohse, F. Lofink, S. Chemnitz, H. Kohlstedt, L. Kienle, and B. Wagner, "Identifying and overcoming the interface originating c-axis instability in highly Sc enhanced AlN for piezoelectric micro-electromechanical systems," J. Appl. Phys. **122**, 035301 (2017).
[28]D. Wang, P. Musavigharavi, J. Zheng, G. Esteves, X. Liu, M. M. A. Fiagbenu, E. A. Stach, D. Jariwala, and R. H. Olsson III, "Sub-microsecond polarization switching in (Al, Sc)N ferroelectric capacitors grown on complementary metal–oxide–semiconductor-compatible aluminum electrodes," Phys. Status Solidi RRL **15**, 2000575 (2021).
[29]G. Esteves, T. R. Young, Z. Tang, S. Yen, T. M. Bauer, M. D. Henry, and R. H. Olsson, "$Al_{0.68}Sc_{0.32}N$ Lamb wave resonators with electromechanical coupling coefficients near 10.28%," Appl. Phys. Lett. **118**, 171902 (2021).
[30]C. Moe, R. Olsson, P. Patel, Z. Tang, M. D'Agati, M. Winters, R. Vetury, and J. Shealy, "Highly doped AlScN 3.5 GHz XBAW resonators with 16% k2eff for 5G RF filter applications," in *2020 IEEE International Ultrasonics Symposium (IUS)* (IEEE, 2020), pp. 1–4.
[31]R. W. Boyd, *Nonlinear Optics*, 3rd ed. (Academic Press, 1992).
[32]B. E. A. Saleh and M. C. Teich, in *Fundamentals of Photonics*, 3rd ed. (John Wiley & Sons, 1991), Chap. 22.
[33]M. Baeumler, Y. Lu, N. Kurz, L. Kirste, M. Prescher, T. Christoph, J. Wagner, A. Žukauskaitė, and O. Ambacher, "Optical constants and band gap of wurtzite $Al_{1-x}Sc_xN/Al_2O_3$ prepared by magnetron sputter epitaxy for scandium concentrations up to x = 0.41," J. Appl. Phys. **126**, 045715 (2019).
[34]M. C. Larciprete, A. Bosco, A. Belardini, R. Li Voti, G. Leahu, C. Sibilia, E. Fazio, R. Ostuni, M. Bertolotti, A. Passaseo, B. Potì, and Z. Del Prete, "Blue second harmonic generation from aluminum nitride films deposited onto silicon by sputtering technique," J. Appl. Phys. **100**, 023507 (2006).
[35]Y. Fujii, S. Yoshida, S. Misawa, S. Maekawa, and T. Sakudo, "Nonlinear optical susceptibilities of AlN film," Appl. Phys. Lett. **31**, 815–816 (1977).
[36]R. H. Olsson, Z. Tang, and M. D'Agati, "Doping of aluminum nitride and the impact on thin film piezoelectric and ferroelectric device performance," in *2020 IEEE Custom Integrated Circuits Conference (CICC)* (IEEE, 2020), pp. 1–6.
[37]R. Deng, S. R. Evans, and D. Gall, "Bandgap in $Al_{1-x}Sc_xN$," Appl. Phys. Lett. **102**, 112103 (2013).
[38]S. Zhu, Q. Zhong, N. Li, T. Hu, Y. Dong, Z. Xu, Y. Zhou, Y. H. Fu, and N. Singh, "Integrated ScAlN photonic circuits on silicon substrate," in 2020 Conference on Lasers and Electro-Optics (CLEO), 2020.
[39]J. Wright, C. Moe, A. V. Sampath, G. A. Garrett, and M. Wraback, "Fabrication of periodically poled AlN with sub-micron periods," Phys. Status Solidi C **8**, 2331–2333 (2011).
[40]W. Zhu, J. Hayden, F. He, J.-I. Yang, P. Tipsawat, M. D. Hossain, J.-P. Maria, and S. Trolier-McKinstry, "Strongly temperature dependent ferroelectric switching in AlN, $Al_{1-x}Sc_xN$, and $Al_{1-x}B_xN$ thin films," Appl. Phys. Lett. **119**, 062901 (2021).
[41]S. Yasuoka, T. Shimizu, A. Tateyama, M. Uehara, H. Yamada, M. Akiyama, Y. Hiranaga, Y. Cho, and H. Funakubo, "Effects of deposition conditions on the ferroelectric properties of $(Al_{1-x}Sc_x)N$ thin films," J. Appl. Phys. **128**, 114103 (2020).
[42]D. Wang, J. Zheng, P. Musavigharavi, W. Zhu, A. C. Foucher, S. E. Trolier-McKinstry, E. A. Stach, and R. H. Olsson III, "Ferroelectric switching in sub-20 nm aluminum scandium nitride thin films," IEEE Electron Device Lett. **41**, 1774–1777 (2020).
[43]W. S. M. Werner, K. Glantschnig, and C. Ambrosch-Draxl, "Optical constants and inelastic electron-scattering data for 17 elemental metals," J. Phys. Chem. Ref. Data **38**, 1013–1092 (2009).